Materials Advances

ROYAL SOCIETY OF CHEMISTRY

PERSPECTIVE

View Article Online
View Journal

Cite this: DOI: 10.1039/d6ma00393a

Toward system-level energy density enhancement in solid oxide cells through 3D structural design

Jinsu Kim *[a] and Inyoung Jang *[b]

As the demand for clean energy systems rises with increasing electricity consumption, solid oxide cells (SOCs) emerge as one of the major energy conversion technologies owing to their high efficiency, fuel flexibility, and compatibility with hybrid systems. Such features position SOCs as promising energy conversion systems for stationary power generation and heavy-duty transportation. However, their broader deployment, particularly in aircraft, is constrained by limited system-level energy conversion density, since excessive mass and volume reduce propulsion efficiency and increase costs, highlighting the need for further improvements in overall system efficiency. While most prior efforts have focused on materials development to improve electrochemical performance, geometric optimization provides an alternative pathway to enhance volumetric and gravimetric power density without relying on new or high-cost material systems. Here, we present a structure-driven perspective that links three-dimensional (3D) SOC geometries to stack-level energy conversion efficiency, mass and volume efficiency, and overall system economics. By analyzing reported 3D geometries for SOCs, we highlight how increased surface-to-volume ratios and reduced stack-component mass fractions can substantially improve system-level energy conversion density while lowering cost metrics. This work shifts the focus of SOC advancement from a material-centric approach toward integrated structure–manufacturing–system design, positioning 3D structural strategies as scalable pathways toward high-energy-density, lightweight SOC systems.

Received 20th March 2026,
Accepted 19th May 2026

DOI: 10.1039/d6ma00393a

rsc.li/materials-advances

1. Introduction

As digital technologies advance, global electricity demand is rapidly increasing, requiring highly efficient and sustainable energy conversion systems. Solid oxide fuel cells (SOFCs) and solid oxide electrolyzer cells (SOECs), together referred to as solid oxide cells (SOCs), are promising technologies for addressing the growing electricity demand owing to their high energy conversion efficiency. In fuel-cell mode, their gas-to-electricity conversion efficiency can reach 60–65%, which is the highest among all fuel-cell types, due to their high operating temperature.[1–3] Moreover, SOC systems offer high fuel flexibility for power generation. While hydrogen is the most commonly used fuel,[4] SOCs can also operate on other fuels such as NH_3 and CH_4, either directly or *via* internal reforming within the support layer.[5–7] In addition, SOCs provide operational flexibility, as they can function in electrolysis mode when operated in reverse, producing H_2 and O_2 from H_2O. This capability further enables the synthesis of various e-fuels, including NH_3 and CH_4.[8] Together, this fuel and operational flexibility allows SOCs to be integrated effectively with renewable energy sources by mitigating intermittency, functioning as both auxiliary energy conversion devices and energy-storage systems.[9–11]

Beyond standalone operation, SOC systems can be integrated with other energy sources, such as gas turbines and nuclear power systems, to enhance overall system efficiency. In particular, integration with gas turbines enables effective utilization of high-temperature exhaust heat, increasing the overall system efficiency from that of standalone SOCs to about 75–80% in hybrid configurations, which makes SOFC systems more favorable for on-site stationary power generation.[12–14] As data centers increasingly require reliable and rapidly deployable energy to support the advancement of AI technologies, SOFC systems are emerging as critical infrastructure for stationary power generation, offering a sustainable and reliable energy solution.

Moreover, advances in high-efficiency SOCs and their hybridization with gas turbine-based systems could substantially contribute to reducing greenhouse gas emissions from aircraft, which account for a significant and growing share of global emissions.[14] However, a key challenge in integrating SOC systems into aircraft is improving energy conversion density, as additional system weight directly reduces overall efficiency due to increased propulsion energy demand. Therefore, achieving high energy conversion density with minimal system weight and volume is important for their applications across various sectors, particularly in aviation

[a] Department of Petrochemical Materials, Chonnam National University, 50 Daehak-ro, Yeosu-si 59631, Republic of Korea. E-mail: jinsu.kim@jnu.ac.kr
[b] School of Chemical and Biomolecular Engineering, Georgia Institute of Technology, Atlanta, GA 30332, USA. E-mail: inyoung.jang@chbe.gatech.edu

and heavy-duty transportation applications such as trucks, ships, and submarines.

Considerable efforts have been made to improve SOCs' energy conversion efficiency and density through the development of high-performance electrode materials (catalysts) to reduce overpotentials during electricity generation; however, the development of new materials often requires extensive long-term validation to address durability and degradation concerns and often relies on expensive rare-earth elements such as Pr, Nd, and Sm, as well as transition metals such as Co.[1,15]

An alternative and potentially more effective strategy to enhance system-level energy conversion density is the development of three-dimensional (3D) SOC architectures. 3D SOC designs can increase the number of electrochemically active reaction sites per unit volume, and because stack components dominate the overall system weight, this approach can substantially improve gravimetric energy conversion (power) density on a kW kg^{-1} basis. In addition, by designing geometries with higher surface-to-volume ratios, the volumetric energy conversion density (kW cm^{-3}) can be further enhanced as shown in Fig. 1. Achieving the same volumetric power density with a smaller system footprint reduces the required size of module components per kW of power generation, ultimately lowering overall stack module costs. Moreover, since the thermal energy required to heat a given system volume to operating temperature remains unchanged, 3D geometries that increase volumetric power density can enhance net energy output per unit thermal energy input. Consequently, the relative contribution of thermal penalties to the overall system energy generation is expected to be reduced, thereby leading to improved system-level performance.

3D structured SOCs can be fabricated using additive manufacturing techniques such as fused filament fabrication (FFF), stereolithography (SLA), digital light processing (DLP), and direct ink writing (DIW).[16] For higher resolution and printing microstructured layers (*e.g.*, electrolytes), micro-SLA or inkjet printing can be utilized.[17,18] These methods enable the fabrication of sophisticated 3D structures, as well as scalable continuous production processes, which can improve the production efficiency of SOCs. However, their major drawback is relatively slow printing speed, which leads to high fabrication costs. For lower-cost and faster production of 3D-structured SOCs, extrusion-based manufacturing methods also represent an effective alternative for fabricating relatively simple 3D structures. However, these approaches offer limited flexibility in geometric design and modification, especially for complex structures such as triply periodic minimal surfaces (TPMS).

Here, to enable the broad application of SOCs in stationary power systems and heavy-duty transportation, we provide an overview of the impact of SOC geometry on energy conversion density in both volumetric and gravimetric terms. Furthermore, this perspective shifts the focus from conventional cell-level performance metrics to a structure–manufacturing–system economics framework that directly links geometric design to system efficiency and the levelized cost of energy (LCOE).

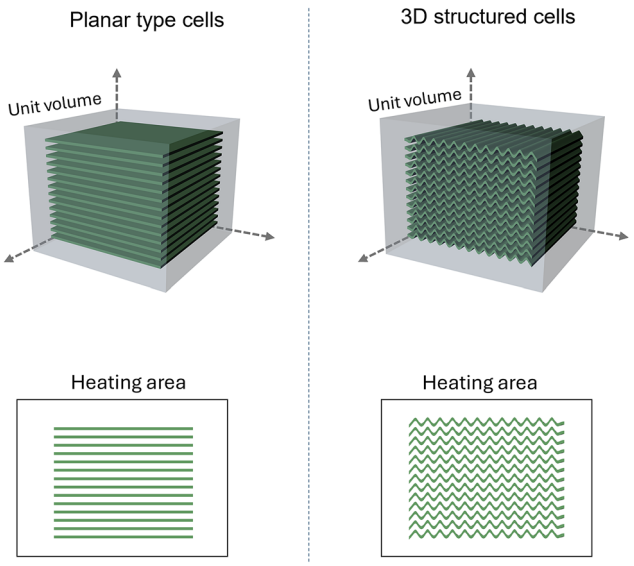

Fig. 1 Schematic illustration of the design of SOCs with higher surface area per unit volume (m^2 m^{-3}).

2. Discussion

2.1. Current energy density of commercial SOC systems and 3D structured cells

Several SOC stack- and module-scale systems have already been commercialized, and most of these are based on planar cell structures, which are more amenable to mass production under current manufacturing practices. As mentioned earlier, for the potential expansion of SOC systems to various applications, such as heavy-duty transportation, and for improving cost-effectiveness by reducing the price of stack components, volumetric and gravimetric power densities serve as key indicators for evaluating the efficiency and performance of system-scale modules. Accordingly, the stack-scale characteristics of commercialized SOFC products, as well as their gravimetric and volumetric power densities, are summarized in Table 1.

As shown in the table, single-unit or large-scale module systems, which include the weight of the reformer and other balance-of-plant components, are typically designed for stationary energy applications. Hence, their gravimetric and volumetric power densities are lower than those of stack-level products.

For large-scale SOFC systems used in stationary power generation, increases in volumetric and gravimetric power density reduce the required mass and volume of auxiliary components, as well as stack components such as end plates, interconnects, current collectors, and sealants. This reduction is expected to lower SOFC stack manufacturing costs and thus decrease the LCOE expected from the SOFC systems. Hence, improvements in both volumetric and gravimetric power density are expected to be advantageous for system advancement and could be achieved through the introduction of 3D structured geometry cells.

To date, various 3D geometries for SOFCs have been reported to enhance the effective surface area per unit volume and increase the density of reaction sites, including gyroidal, monolithic,

Table 1 Reported specific electrical energy conversion performance of SOFC stacks with planar cells (commercialized stack scale)

	Output power/kW	Gravimetric power density/kW kg^{-1}	Volumetric power density/W cm^{-3}	Operating temperature/°C	Ref.
Hyfindr	4.1	—	0.387	650–750	19
Lentatek	1–1.3	0.052	0.194	780–820	20
Elcogen	3	0.091	0.245	580–720	21
Doosan (Ceres)	5.75	—	0.443	600	22
Kyocera	0.7	0.14	0.118	—	23
Morimura[a]	0.6	0.013	0.006	—	24
Daigas/Ene-farm S[a]	0.7	0.008	0.003	—	25
Bloom Energy[b]	325	0.025	0.011	—	26

[a] Single-module scale. [b] Large-size system scale, which is an assembly of stack modules.

tubular, wave, and pillar-shaped electrodes. Table 2 summarizes the reported volumetric and gravimetric power densities of these 3D-structured SOFCs, along with their corresponding peak areal power densities for each structure.

These 3D cell architectures are expected to be highly effective in enhancing both gravimetric and volumetric power densities, although most reported designs remain at the cell scale. Collins *et al.* reported a projected system-scale energy density for a monolithic stack design that eliminates metal interconnects, with an estimated gravimetric power density of 4.6 kW kg^{-1};[33] however, experimental development and validation are still required. Similarly, cell designs based on the gyroidal geometries and lightweight tubular structures in Table 2 also have strong potential to minimize the use of metal interconnects at the stack level. Beyond the projected power-density advantages, recent durability studies indicate that 3D-structured SOCs can sustain long-term operation comparable to, or in some cases exceeding, conventional planar designs. Reported degradation rates include 0.69% kh^{-1} over 1000 h for a monolithic flat-tubular stack,[34] 0.58% kh^{-1} over 1500 h with 1000 thermal cycles for a 3D-printed microtubular cell,[35] and 0.093% kh^{-1} over 5218 h for a microtubular cell with an optimized anode buffer layer.[36] Although early monolithic metal-supported designs suffered from rapid failure, processing optimizations have improved durability by up to two orders of magnitude,[37] indicating that the long-term stability of 3D structures is primarily limited by manufacturing quality rather than the structure itself. In addition, recent polarization-based degradation models further enable quantitative lifetime prediction of such complex cells.[38] Therefore, the currently reported gravimetric power densities (*e.g.*, ~1.1–2 kW kg^{-1}) for these architectures are not expected to decline substantially with further scale-up to the stack level.

These 3D structured SOFCs would be especially advantageous for applications in heavy-duty transportation, particularly in aircraft, where high energy conversion density systems integrated with gas turbines are required. SOC systems can offer higher energy conversion density than conventional energy-storage technologies, such as batteries (~0.3 kWh kg^{-1}), by utilizing high-energy-density fuels such as H_2 and CH_4, which have gravimetric energy densities of about 40 kWh kg^{-1} and 16 kWh kg^{-1} in the liquid form, respectively.[39,40] A hybrid gas turbine–SOFC–battery system design introduced by Collins and McLarty exhibited an expected energy density of 7 kWh kg^{-1} and a power density of 0.9 kW kg^{-1} through the integration of high gravimetric power density SOFC systems. These projected energy and power densities are potentially sufficient for operating medium- and long-range aircraft.[33] For spacecraft implementation, however, higher performance targets are required, with gravimetric power densities exceeding 1 kW kg^{-1}.[27,41]

2.2. Geometry-driven volumetric performance and economic impact

Table 3 presents a comprehensive geometry-driven performance propagation framework that systematically quantifies how geometric design choices cascade across multiple length scales to determine system-level performance in SOCs. The framework goes beyond cell-level electrochemical metrics by linking structural parameters to volumetric characteristics and economic outcomes. The analysis starts by examining geometric descriptors such as

Table 2 Specific electrical energy conversion performance of SOFCs with 3D structures

	Output power/W	Gravimetric power density/kW kg^{-1}	Volumetric power density/W cm^{-3}	Areal peak power density/W cm^{-2}	Operation temperature/°C	Ref.
Gyroidal shape		~1.10	4.0	0.45	900	27
Monolith shape	—	—	5.6	0.475	780	28
Tubular	5.4 per tube	0.35/0.1[a]	0.27	0.4	750	29
Light weight tubular		2	—	~0.63	750	30
Wave shape	9 per unit	—	1[b]	0.2	900	31
Pillar shape	0.91[c]	—	6.1[d]	0.92	800	32

All values were calculated at the cell scale, except the value marked with subscript a, which was calculated at the system scale considering stack or system components. Values marked with subscripts b–d were derived from the reported peak power density and the active area or cell thickness reported in the reference papers. The geometrical parameters used in these calculations are provided in the Notes. [a] System scale. [b] Calculated based on the cell thickness of 2 mm. [c] Electrode area of 1 cm^2. [d] Calculated based on the cell thickness of 1.5 mm including pillars.

Table 3 Geometry-driven performance propagation framework for solid oxide cells

Category	Parameter (unit)	2D planar	3D gyroid	3D micropillar
Geometry descriptors		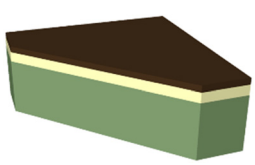	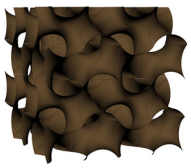	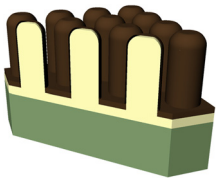
	Specific surface area (m^2 m^{-3})	10–50[a]	80–200[44]	60–120[b]
	Surface utilization factor (—)[c]	0.45–0.70	0.30–0.65	0.22–0.54
	Effective surface area (m^2 m^{-3})[d]	6–30	36–90	21–42
Cell-level physics	Thermal-neutral voltage (V)	Shared value range, $H_2 + \frac{1}{2}O_2 \rightleftarrows H_2O$, 700 °C: 1.284 V, 800 °C: 1.287 V[45]		
	Area-specific resistance (Ω cm^2)[e]	~0.25–0.45 at 800 °C[46,47]		
	Peak power density (W cm^{-2})[f]	0.92–1.66 at 700–800 °C		
Unit-volume performance	Volumetric power density (W cm^{-3})	0.055–0.498	0.331–1.494	0.139–0.697
	Mass-specific power throughput (kW kg^{-1})[g]	0.023–0.208	0.148–0.831	0.064–0.233
	Pressure drop (Pa m^{-1})[h]	1000–3000	300–800	3000–8000
	P_{net}/P_{gross} (—)	0.986–0.989		
	P/V_{stack} (kW L^{-1})	0.276	0.910	0.444
	Net electrical efficiency (LHV) (—)[i]	0.566–0.572		
	Levelized cost of electricity (US$ per kWh)[j]	0.11–0.30	0.07–0.19	0.09–0.25

[a] For planar SOCs, the surface-to-volume ratio is defined as the inverse of the stacking repeat length.[48] [b] For micropillar structures, A/V is evaluated as $1/L_{stack}$ plus the pillar sidewall contribution, based on representative pillar geometries (d = 8–12 μm, h = 20–50 μm, p = 30–50 μm) and stack repeat lengths (L_{stack} = 15–30 mm). [c] Defined as the porosity-to-tortuosity ratio representing transport-mediated surface accessibility. [d] Representative values of the transport accessibility factor ($=\varepsilon/\tau$) are assumed for structure-level comparison, with void fraction (ε) and tortuosity (τ) taken as follows: planar (ε = 0.6, τ = 1.0),[49] gyroid (ε = 0.7, τ = 1.5),[16] and micropillar (ε = 0.5, τ = 1.4).[50] [e] Area-specific resistance is defined as the slope of the linear, ohmic-dominated region of the polarization curve. Representative values correspond to operation at 800 °C and are treated as geometry-independent material parameters for structure-level performance propagation. [f] Peak power density is analytically derived assuming an ohmic-dominated linear polarization behavior, representing an ohmic-limited upper-bound estimate used for structure-level scaling (E_{rev} denotes the reversible cell voltage at the specified temperature). [g] Mass is estimated from the solid fraction of the active cell structure, excluding balance-of-stack components. A representative solid density of yttria-stabilized zirconia is used (ρ_{solid} = 5.99 g cm^{-3}, 8YSZ theoretical density).[51] [h] Pressure drop gradient per unit flow path length at 700–800 °C, excluding manifold losses. Planar,[52] gyroidal,[53] and micropillar[54] values based on CFD and experimental data for respective channel geometries. [i] Net electrical efficiency and hydrogen consumption are calculated on an LHV basis assuming H_2–O_2 fuel cell operation with 85% fuel utilization. [j] Levelized cost of electricity for planar SOFCs: US$ 0.11–0.30 kWh^{-1} at the kW-to-MW scale.[55,56]

effective surface area and the surface utilization factor, which reflect the structural characteristics of 2D planar, 3D gyroidal, and 3D micropillar designs. These geometric descriptors are then translated into electrochemical parameters using an ohmic-dominated analytical model. In this model, area-specific resistance (ASR) is treated as a geometry-independent material property with typical values of 0.25–0.45 $\Omega \cdot cm^2$ at 800 °C, while the peak areal power density is calculated from the maximum power condition ($dP/dj = 0$) under ohmic-dominated polarization behavior. The framework then translates these electrochemical metrics into volumetric and mass-specific performance indicators by incorporating the effective surface area. This parameter is calculated as the product of geometric surface area and transport accessibility, directly determining the active reaction zone density within a given stack volume. This hierarchical approach allows for systematic comparison of how different architectures affect electrochemical performance, system compactness, and material efficiency. The results reveal that 3D gyroidal structures deliver volumetric power densities of 0.331–1.494 W cm^{-3}, approximately 3–6 times higher than those of conventional 2D planar cells. This enhancement stems from the higher effective surface area afforded by the TPMS-based geometry. The superior volumetric characteristics enable significant process intensification, with gyroidal structures requiring approximately one-third the volume of planar configurations. The gyroidal structure shows the lowest dP (planar: 1000–3000 Pa m^{-1}; micropillar: 3000–8000 Pa m^{-1}). Despite these differences, all structures achieve similar net efficiencies (~94.5–94.9%), as parasitic losses associated with auxiliary components remain below 1.5% of the total generated power. These parasitic loads range from a minimum of 1.1% for the gyroidal structure to a maximum value in the micropillar design, primarily due to differences in pressure drop within the flow channels. The net efficiency slightly increases, suggesting that gains in electrical output per unit thermal energy input remain limited. This is likely because the auxiliary systems already consume relatively little energy, contrary to the initial expectation. Meaningful system-level economic benefits still emerge from architectural optimization. The more compact gyroidal form factor reduces volume-dependent capital expenditure, resulting in a potential reduction of up to 20–30% in LCOE as shown in Fig. 2. This cost advantage is driven primarily by reduced material use, modular scalability, and lower balance-of-plant integration effort rather than by electrochemical performance gains. This estimate is further supported by recent reports of concrete manufacturing-cost reductions specific to 3D-printed SOCs, including 37–97% material savings *via* replacement of metallic interconnects with printed ceramic counterparts[42] and consolidation of the conventional multi-step ceramic process into a single-step printing and co-sintering route.[43]

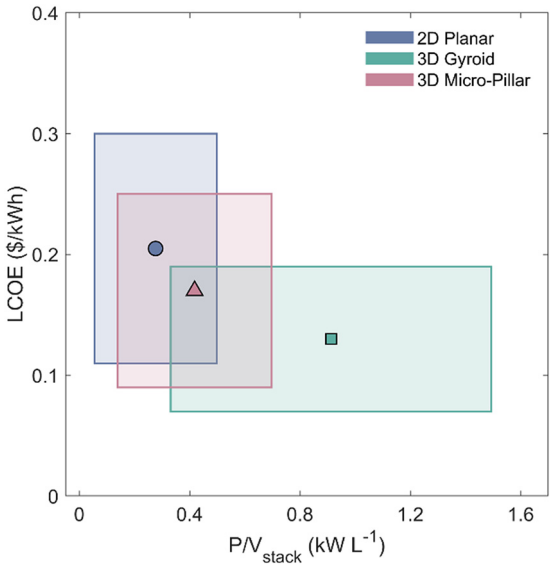

Fig. 2 Relationship between stack compactness and projected LCOE.

3. Conclusion

In this perspective, we have reported a high-level assessment of 3D-structured SOCs, analyzing their projected advantages in system efficiency and cost-effectiveness, as well as their geometric development pathways at the system scale. The geometry-driven analysis reveals that 3D structures can deliver 3–6 times higher volumetric and gravimetric power densities, offering a viable pathway toward improved system-level performance in electricity generation. At the system level, pressure-drop effects across planar and 3D geometries are found to be negligible, indicating that the structural complexity does not introduce substantial aerodynamic penalties. However, despite the substantially higher active-area density, improvements in volumetric heat utilization remain modest, resulting in limited gains in net efficiency. Nevertheless, the projected LCOE shows a potential reduction of up to 20–30% for 3D structures, mainly driven by lower system manufacturing costs enabled by enhanced power densities. Such geometry-driven cost reduction strategies position 3D SOCs as promising candidates not only for reducing stationary power generation costs but also for enabling applications in the aviation sector.

Ultimately, shifting the design paradigm from material-centric optimization to a structure–manufacturing–system economics framework enables a more direct linkage between cell geometry and real-world deployment metrics. By leveraging stable and commercially mature materials while optimizing 3D architectures, SOC systems can advance toward higher energy conversion density, lower capital intensity, and broader applicability across stationary power, ground transportation, and aerospace sectors. Lowering the manufacturing costs of 3D-structured SOCs, particularly those produced *via* 3D printing, remains an important step toward improving the practical viability of these architectures. As 3D printing scales up to industrial production, fabrication costs are expected to decline due to economies of scale, as well as continued technological advancements. At the same time, alternative low-cost fabrication methods, including extrusion-based processing, can provide additional pathways toward cost-effective implementation. However, as mentioned in the introduction, extrusion-based methods have limitations in the achievable structural complexity. Therefore, hybrid fabrication approaches are required for the fabrication of complex geometries such as TPMS.

Throughout the manuscript, we focus on the effects of 3D geometry on system efficiency, cost, and energy density. In addition to structural design, incorporating advanced materials can further reduce ohmic and polarization resistances compared to conventional LSC|YSZ|YSZ–Ni cells, particularly in electrolyte-supported configurations. 3D structures, such as gyroidal or wave-type structures, are typically based on electrolyte-supported cells that use thick YSZ as a mechanically robust backbone onto which electrode materials are coated on both sides. The electrolyte layer can be replaced with materials exhibiting higher oxide-ion conductivity, such as GDC, LSGM, or proton conducting oxides, which exhibit ionic conductivities about an order of magnitude higher than that of YSZ. However, these materials still suffer from electronic leakage, leading to performance degradation and reduced stability; therefore, further efforts are required to improve their long-term reliability. In addition, material advancements can be directed toward reducing polarization resistance at lower operating temperatures through optimization of air- and fuel-electrode materials. For low-cost manufacturing, these material engineering strategies should also consider both material cost and long-term reliability to ensure overall system competitiveness for practical deployment as a future energy system.

Alternatively, the electrolyte-supported configuration can be replaced by an anode-supported design, for example, by printing the 3D structure using NiO–YSZ electrode materials, enabling the coating of a thinner electrolyte layer. However, for TPMS structures such as gyroid and Fischer–Koch S, where the supporting structure serves both as a mechanical support and as a gas transport pathway, effective separation of fuel and air streams across the thin electrolyte layer must be maintained. This requires geometric design optimization to create two different gas channels, as well as improved coating strategies for forming a uniform electrolyte layer within the complex 3D geometries.

Future efforts should focus on scalable and low-cost manufacturing routes for complex 3D geometries, experimental validation at the stack scale, and integration studies within hybrid turbine-based platforms. With these developments, structure-driven SOC design may represent a decisive step toward high-energy conversion efficiency, volume-efficient, and economically competitive energy conversion systems.

Conflicts of interest

There are no conflicts to declare.

Abbreviations

A	Geometric surface area (architecture-relevant surface) (m^2)

ASR	Area-specific resistance (ohmic-dominated slope) (Ω cm^2)
CAPEX	Total capital expenditure (US$)
$\mathrm{CAPEX_{ref}}$	Reference capital expenditure (US$)
$\mathrm{CAPEX_{an}}$	Annualized CAPEX (US$ per year)
C_{fuel}	Fuel unit cost (US$ per MJ)
CRF	Capital recovery factor
$C_{\mathrm{p,eff}}$	Effective specific heat capacity of the hot-zone (J g^{-1} K^{-1})
$\mathrm{d}P/\mathrm{d}J$	Derivative of areal power density with respect to current density (W A^{-1})
$\mathrm{d}P/\mathrm{d}L$	Pressure-drop gradient along the flow path (Pa m^{-1})
E_{an}	Annual net electricity generation (kWh per year)
E_{rev}	Reversible (Nernst) cell voltage (V)
E_{therm}	Effective specific heat capacity of stack (J)
$f_{\mathrm{O\&M}}$	O&M fraction of CAPEX
f_{aux}	Fixed auxiliary fraction of gross power
f_{loss}	Fraction of the hot-zone thermal inventory energy that must be externally supplied to account for start-up heating and ongoing temperature maintenance during the reference duty window
$f_{\mathrm{parasitic}}$	Parasitic fraction
F	Faraday constant (C mol^{-1})
I_{stack}	Stack current corresponding to P_{gross} at V_{cell} (A)
i	Discount rate
j	Current density (A cm^{-2})
j_{peak}	Peak-power current density in the ohmic model (A cm^{-2})
L_{flow}	Flow-path length used for pressure-drop scaling (m)
LCOE	Levelized cost of electricity (US$ per kWh)
$\mathrm{LCOE_{ref}}$	Reference LCOE (US$ per kWh)
$\mathrm{LHV_{fuel}}$	Lower heating value of the fuel (J kg^{-1})
m_{fuel}	Fuel mass flow rate (kg s^{-1})
$m_{\mathrm{fuel,an}}$	Annual fuel consumption (kg per year)
N_{y}	Operation lifetime (year)
n	Number of electrons transferred per reaction as used in the V_{TN} definition
$\mathrm{OPEX_{an}}$	Total annual operating expenditure (US$ per year)
$\mathrm{OPEX_{elec,an}}$	Annual electricity cost (US$ per year)
$\mathrm{OPEX_{therm,an}}$	Annual thermal cost (US$ per year)
$\mathrm{OPEX_{O\&M,an}}$	Annual O&M cost (US$ per year)
P_{blower}	Blower electrical power for flow delivery (W)
P_{gross}	Gross electrical power basis (fixed system power target) (W)
P_{net}	Net electrical power output (W)
$P_{\mathrm{parasitic}}$	Total parasitic power (W)
P_{peak}	Peak areal power density from the ohmic-limited model (W cm^{-2})
$P_{\mathrm{mass,peak}}$	Peak mass-specific power throughput (W g^{-1})
$P_{\mathrm{vol,peak}}$	Peak volumetric power density (W cm^{-3})
$\mathrm{SEC_{sys}}$	Total specific energy consumption (kWh $\mathrm{kg_{H_2}}^{-1}$)
$t_{\mathrm{op,an}}$	Annual operating time (h per year)
$V(j)$	Cell voltage as a function of current density in the linear (ohmic) regime (V)
V_{cell}	Operating cell voltage used for system sizing (V)
V_{stack}	Required stack (active) volume to meet P_{gross} (cm^3)
V_{TN}	Thermoneutral voltage (V)
V_{unit}	Unit-cell (architecture repeat) volume used in A/V descriptors (cm^3)
$\dot{V}$	Total volumetric flow rate through the system (m^3 s^{-1})
ΔH_{rxn}	Reaction enthalpy change for V_{TN} (J mol^{-1})
ΔP	Pressure drop across the flow path (Pa)
α	CAPEX scaling exponent (0.6–0.8)
ε	Porosity (void fraction) used for the solid fraction
η_{blower}	Blower (fan/compressor) efficiency
η_{BOP}	Balance-of-plant efficiency multiplier
$\eta_{\mathrm{elec,LHV}}$	Fuel-to-electric efficiency (LHV basis)
Φ	Normalized cost ratio
ρ_{eff}	Effective density of the stack (g cm^{-3})
ρ_{solid}	Solid density of the architecture material (g cm^{-3})
τ	Tortuosity (transport path lengthening factor)
ω	CAPEX portion in LCOE

Data availability

All references and websites from which the data were obtained are listed in the References section. No primary research results, software, or code were generated as part of this perspective. All analyses and equations are presented in the main manuscript.

Appendix

The complete set of equations used in the architecture-driven performance propagation framework, which sequentially translates geometric descriptors into cell-level electrochemical parameters, volumetric performance metrics, system-level energy consumption, and economic indicators, is given below.

$$\left(\frac{A}{V_{\mathrm{unit}}}\right)_{\mathrm{eff}} = \left(\frac{A}{V_{\mathrm{unit}}}\right)\left(\frac{\varepsilon}{\tau}\right) \tag{A1}$$

$$V(j) = E_{\mathrm{rev}} - j\mathrm{ASR} \tag{A2}$$

$$\frac{\mathrm{d}P}{\mathrm{d}j} = 0 \tag{A2a}$$

$$j_{\mathrm{peak}} = \frac{E_{\mathrm{rev}}}{2\mathrm{ASR}} \tag{A2b}$$

$$P_{\mathrm{peak}} = \frac{{E_{\mathrm{rev}}}^2}{4\mathrm{ASR}} \tag{A2c}$$

$$P(j) = jV(j) \tag{A3}$$

$$V_{\mathrm{TN}} = \frac{\Delta H_{\mathrm{rxn}}}{nF} \tag{A4}$$

$$P_{\mathrm{vol,peak}} = P_{\mathrm{peak}}\left(\frac{A}{V_{\mathrm{unit}}}\right)_{\mathrm{eff}} \tag{A5}$$

$$P_{\mathrm{mass,peak}} = \frac{P_{\mathrm{vol,peak}}}{(1-\varepsilon)\rho_{\mathrm{solid}}} \quad \text{(A6)}$$

$$V_{\mathrm{stack}} = \frac{P_{\mathrm{gross}}}{P_{\mathrm{vol,peak}}} \quad \text{(A7)}$$

$$I_{\mathrm{stack}} = \frac{P_{\mathrm{gross}}}{V_{\mathrm{cell}}} \quad \text{(A8)}$$

$$\Delta P = \left(\frac{\mathrm{d}P}{\mathrm{d}L}\right) L_{\mathrm{flow}} \quad \text{(A9)}$$

$$P_{\mathrm{blower}} = \frac{\dot{V}\Delta P}{\eta_{\mathrm{blower}}} \quad \text{(A10)}$$

$$P_{\mathrm{parasitic}} = P_{\mathrm{blower}} + f_{\mathrm{aux}} P_{\mathrm{gross}} \quad \text{(A11)}$$

$$f_{\mathrm{parasitic}} = \frac{P_{\mathrm{parasitic}}}{P_{\mathrm{gross}}} \quad \text{(A12)}$$

$$P_{\mathrm{net}} = P_{\mathrm{gross}}(1 - f_{\mathrm{parasitic}}) \quad \text{(A13)}$$

$$\eta_{\mathrm{elec,LHV}} = \frac{P_{\mathrm{net}}}{\dot{m}_{\mathrm{fuel}} \mathrm{LHV}_{\mathrm{fuel}}} \quad \text{(A14)}$$

$$E_{\mathrm{an}} = P_{\mathrm{net}} t_{\mathrm{op,an}} \quad \text{(A15)}$$

$$\mathrm{LCOE}_{\mathrm{ref}} \equiv \text{literature-based levelized cost} \quad \text{(A16)}$$

$$\Phi = \frac{\mathrm{LCOE}}{\mathrm{LCOE}_{\mathrm{ref}}} \quad \text{(A17)}$$

$$r = \frac{V_{\mathrm{stack}}}{V_{\mathrm{stack,ref}}} \quad \text{(A18)}$$

$$\mathrm{CAPEX} = \mathrm{CAPEX}_{\mathrm{ref}} r^{\alpha} \quad \text{(A19)}$$

$$\mathrm{CRF} = \frac{i(1+i)^{N_{\mathrm{yr}}}}{(1+i)^{N_{\mathrm{yr}}} - 1} \quad \text{(A20)}$$

$$\mathrm{OPEX}_{\mathrm{fuel,an}} = C_{\mathrm{fuel}} m_{\mathrm{fuel,an}} \quad \text{(A21)}$$

$$m_{\mathrm{fuel,an}} = t_{\mathrm{op,an}} \dot{m}_{\mathrm{fuel}} \quad \text{(A22)}$$

$$\mathrm{OPEX}_{\mathrm{o\&m}} = f_{\mathrm{o\&m}} \mathrm{CAPEX} \quad \text{(A23)}$$

$$\mathrm{LCOE} = \frac{\mathrm{CAPEX}_{\mathrm{an}} + \mathrm{OPEX}_{\mathrm{an}}}{E_{\mathrm{an}}} \quad \text{(A24)}$$

$$\Phi \cong \omega_{\mathrm{capex}} r^{\alpha} + (1 - \omega_{\mathrm{capex}}) \frac{\mathrm{OPEX}_{\mathrm{an}}}{\mathrm{OPEX}_{\mathrm{an,ref}}} \quad \text{(A25)}$$

Acknowledgements

This study was financially supported by Chonnam National University (grant no. 2024-1966-03).

References

1 I. Jang, J. S. A. Carneiro, J. O. Crawford, Y. J. Cho, S. Parvin, D. A. Gonzalez-Casamachin, J. Baltrusaitis, R. P. Lively and E. Nikolla, *Chem. Rev.*, 2024, **124**, 8233–8306.
2 E. D. Wachsman and K. T. Lee, *Science*, 2011, **334**, 935–939.
3 M. Kinnon, G. Razeghi and S. Samuelsen, *Renewable Sustainable Energy Rev.*, 2021, **147**, 111226.
4 J. Kim, H. Lee, B. Lee, J. Kim, H. Oh, I.-B. Lee, Y.-S. Yoon and H. Lim, *Energy Convers. Manage.*, 2021, **250**, 114922.
5 E. P. Murray, T. Tsai and S. A. Barnett, *Nature*, 1999, **400**, 649–651.
6 S. McIntosh and R. J. Gorte, *Chem. Rev.*, 2004, **104**, 4845–4866.
7 G. Jeerh, M. Zhang and S. Tao, *J. Mater. Chem. A*, 2021, **9**, 727–752.
8 F. Liu, D. Ding and C. Duan, *Adv. Sci.*, 2023, **10**, 2206478.
9 G. Glenk and S. Reichelstein, *Nat. Energy*, 2019, **4**, 216–222.
10 J. Rugolo and M. J. Aziz, *Energy Environ. Sci.*, 2012, **5**, 7151–7160.
11 A. Hauch, R. Küngas, P. Blennow, A. B. Hansen, J. B. Hansen, B. V. Mathiesen and M. B. Mogensen, *Science*, 2020, **370**, eaba6118.
12 P. Talebizadehsardari, K. Hosseinzadeh, H. I. Mohammed, F. L. Rashid, N. Alipour, H. A. Maarof, H. Togun, A. Chattopadhyay, S. Sen and A. Cairns, *Renewable Sustainable Energy Rev.*, 2026, **229**, 116636.
13 H. C. Patel, T. Woudstra and P. V. Aravind, *Fuel Cells*, 2012, **12**, 1115–1128.
14 G. Peyrani, P. Marocco, M. Gandiglio, R. Biga and M. Santarelli, *eTransportation*, 2025, **24**, 100408.
15 Y. Chen, W. Zhou, D. Ding, M. Liu, F. Ciucci, M. Tade and Z. Shao, *Adv. Energy Mater.*, 2015, **5**, 1500537.
16 C. Kim and I. Jang, *J. Phys. Energy*, 2024, **6**, 032003.
17 C. Vidler, K. Crozier and D. Collins, *Microsyst. Nanoeng.*, 2023, **9**, 67.
18 N. M. Farandos, I. Jang, J. C. Alexander and G. H. Kelsall, *Electrochim. Acta*, 2022, **426**, 140834.
19 Solid Oxide Fuel Cell Stack AERIE 120 (4kW) | Hyfindr, https://hyfindr.com/marketplace/components/fuel-cell-stacks/sofc-stacks/solid-oxide-fuel-cell-stack-aerie-120/.
20 Lentatek, Lentatek - Solid Oxide Fuel Cell (SOFC) Stack, https://www.lentatek.com/solutions/hydrogen-and-fuel-cell-technologies/solid-oxide-fuel-cell-sofc-stack.
21 Solid oxide stacks for fuel cell systems, https://elcogen.com/products/solid-oxide-stacks-for-fuel-cell-systems/.
22 PureCell® Model 400 NG, https://www.doosanfuelcell.com/en/prod/prod-0101.
23 SOFC (Solid Oxide Fuel Cell) Stack - Energy Conversion Devices - KYOCERA, https://global.kyocera.com/prdct/ecd/sofc/.
24 Morimura SOFC Technology Co. Ltd, https://www.ngkntk.co.jp/english/news/detail/003004.html.
25 Daigas Group, https://www.daigasgroup.com.
26 Bloom Energy Server Resources, https://www.bloomenergy.com/resources/.
27 Z. Zhou, A. R. Lalwani, X. Sun, Z. Pan, P. Shahriary, Y. Xie, Y. Shang, J. L. Navas, A. Basso, N. Shang, M. Artemeva,

P. Khajavi, M. Chen, V. B. Tinti, D. B. Pedersen, V. K. Nadimpalli and V. Esposito, *Nat. Energy*, 2025, **10**, 962–970.
28 S. Pirou, B. Talic, K. Brodersen, A. Hauch, H. L. Frandsen, T. L. Skafte, Å. H. Persson, J. V. T. Høgh, H. Henriksen, M. Navasa, X.-Y. Miao, X. Georgolamprou, S. P. V. Foghmoes, P. V. Hendriksen, E. R. Nielsen, J. Nielsen, A. C. Wulff, S. H. Jensen, P. Zielke and A. Hagen, *Nat. Commun.*, 2022, **13**, 1263.
29 A. D. Meadowcroft, S. Howroyd, K. Kendall and M. Kendall, *ECS Trans.*, 2013, **57**, 451.
30 P. Nehter, H. Geisler, V. Ahilan, S. Friedl, O. Rohr, A. Walter, C. Metzner and K. Zimmermann, *ECS Trans.*, 2023, **111**, 143.
31 A. M. Martos, S. Márquez, R. S. Pavlov, W. Zambelli, S. Anelli, M. Nuñez, L. Bernadet, J. J. Brey, M. Torrell and A. Tarancón, *J. Power Sources*, 2024, **609**, 234704.
32 I. Jang, A. Hankin, Z. Xie, S. J. Skinner and G. H. Kelsall, *Small*, 2024, **20**, 2306653.
33 J. M. Collins and D. McLarty, *Appl. Energy*, 2020, **265**, 114787.
34 S. Park, N. M. Sammes, K.-H. Song, T. Kim and J.-S. Chung, *Int. J. Hydrogen Energy*, 2017, **42**, 1154–1160.
35 W. Huang, C. Finnerty, K. Wang, R. Sharp and B. Balili, *Int. J. Hydrogen Energy*, 2019, **44**, 32158–32163.
36 Y. Liu, H. Ye, Y. Ma, C. Wang, J. Liu, Y. Liu, X. Xu, Z. Chen and B. Liang, *Int. J. Appl. Ceram. Technol.*, 2024, **21**, 340–348.
37 S. Pirou, B. Talic, K. Brodersen, T. L. Skafte, A. Hauch, J. V. T. Høgh, H. Henriksen, Å. H. Persson and A. Hagen, *Int. J. Hydrogen Energy*, 2023, **48**, 11017–11028.
38 J.-I. Lee, H. Kim, H. Yu, S. Gopalan, S. Basu and U. Pal, *Int. J. Hydrogen Energy*, 2026, **197**, 152614.
39 M. B. Mogensen, M. Chen, H. L. Frandsen, C. Graves, J. B. Hansen, K. V. Hansen, A. Hauch, T. Jacobsen, S. H. Jensen, T. L. Skafte and X. Sun, *Clean Energy*, 2019, **3**, 175–201.
40 N. Gejjiganahalli Ningappa, K. Vishweswariah, S. Ahmed, M. Djihad Bouguern, M. R. A. Kumar and K. Zaghib, *Energy Environ. Sci.*, 2025, **18**, 9786–9838.
41 T. L. Cable and S. W. Sofie, *J. Power Sources*, 2007, **174**, 221–227.
42 V. J. Ferreira, D. Wolff, A. Hornés, A. Morata, M. Torrell, A. Tarancón and C. Corchero, *Appl. Energy*, 2021, **291**, 116803.
43 N. Kostretsova, A. Pesce, S. Anelli, M. Nuñez, A. Morata, F. Smeacetto, M. Torrell and A. Tarancón, *J. Mater. Chem. A*, 2024, **12**, 22960–22970.
44 T. Ott and V. Dreißigacker, *Energies*, 2024, **17**, 5781.
45 M. Lang, S. Raab, M. S. Lemcke, C. Bohn and M. Pysik, *Fuel Cells*, 2020, **20**, 690–700.
46 A. Hauch, S. H. Jensen, S. Ramousse and M. Mogensen, *J. Electrochem. Soc.*, 2006, **153**, A1741.
47 J. Hong, J. Grimes, D. Cox and S. A. Barnett, *Appl. Energy*, 2024, **355**, 122275.
48 D. Udomsilp, C. Lenser, O. Guillon and N. H. Menzler, *Energy Technol.*, 2021, **9**, 2001062.
49 J. R. Wilson, W. Kobsiriphat, R. Mendoza, H.-Y. Chen, J. M. Hiller, D. J. Miller, K. Thornton, P. W. Voorhees, S. B. Adler and S. A. Barnett, *Nat. Mater.*, 2006, **5**, 541–544.
50 J. A. Cebollero, M. A. Laguna-Bercero, R. Lahoz, J. Silva, R. Moreno and A. Larrea, *J. Eur. Ceram. Soc.*, 2019, **39**, 3466–3474.
51 D. Panthi, N. Hedayat and Y. Du, *J. Adv. Ceram.*, 2018, **7**, 325–335.
52 W. J. Sembler and S. Kumar, *J. Fuel Cell Sci. Technol.*, 2010, **8**, 021007.
53 S. S. Rathore, B. Mehta, P. Kumar and M. Asfer, *Transp. Porous Media*, 2023, **146**, 669–701.
54 S. Piedra, A. Gómez-Ortega and J. Pérez-Barrera, *Fluids*, 2023, **8**, 312.
55 R. Scataglini, M. Wei, A. Mayyas, S. H. Chan, T. Lipman and M. Santarelli, *Fuel Cells*, 2017, **17**, 825–842.
56 D. Roy, S. Samanta, S. Roy, A. Smallbone and A. Paul Roskilly, *Green Chem.*, 2024, **26**, 3979–3994.